Electronic Supplementary Information (ESI) for:

Panoramic portrait of primary molecular events preceding excited state proton transfer in water

Weimin Liu,[a] Yanli Wang,[a] Longteng Tang, Breland G. Oscar, Liangdong Zhu and Chong Fang*

Department of Chemistry, Oregon State University, Corvallis, OR 97331-4003 USA

[a]These authors contributed equally to this work.

*To whom correspondence should be addressed. E-mail: Chong.Fang@oregonstate.edu.

This PDF file includes:

ESI Methods

A. Ultrafast Raman Measurements. The femtosecond stimulated Raman spectroscopy (FSRS) setup employs a femtosecond (fs) laser system consisting of a mode-locked Ti:Sapphire oscillator (Mantis-5) and regenerative amplifier (Legend Elite-USP-1K-HE, Coherent, Inc.), which provides the 4 mJ fundamental pulse (FP) centered at 800 nm with 35 fs pulse duration and 1 kHz repetition rate. Half of the output laser beam is split into three beams to generate a tunable picosecond (ps) Raman pump, a broadband fs Raman probe, and an fs actinic pulse to initiate photochemical reactions.

The details of our newly developed tunable FSRS setup for ground-state Stokes Raman measurement have been reported.[1] Briefly, part of the FP at ~1.6 mJ is used to generate the wavelength-tunable Raman pulse based on a two-stage ps noncollinear optical parametric amplifier (NOPA) system. The ps pump pulse for NOPA is generated by a home-built second harmonic bandwidth compressor (SHBC), which utilizes chirp elimination in second harmonic generation (SHG) when the incident FPs have opposite temporal chirps, to produce 400 nm pulses with average power of ~150 mW and pulse duration of ~2 ps. For the tunable ps seed pulses, we first utilize an fs-NOPA system to generate a broadband laser pulse, and the output with average pulse energy of 1 μJ is then dispersed by a reflective grating (1800 grooves/mm, 500 nm blaze at 26.7º) and filtered through an adjustable mechanical slit to generate a ps seed pulse with ~12 cm^{-1} bandwidth. The 400 nm ps pump pulse is divided by a beamsplitter (70%R:30%T), and the ps seed is successively amplified through two type-II BBO crystals by the ps pump pulses in the two-stage ps-NOPA system. The final output is a narrowband (ca. 28 cm^{-1} at 600 nm), tunable (ca. 480—750 nm) Raman pump pulse with an average power of 12 mW. In this work, the center wavelength of Raman pump is tuned to 580 nm with suitable power

(see below for power-dependence measurement) to achieve pre-resonance enhancement[2,3] for transient Raman modes of HPTS in the first singly electronic excited state (S_1).

To generate the actinic pump, FP of ~200 μJ is collimated by a telescope lens system to decrease the beam size and then frequency doubled in a 0.3-mm type-I BBO crystal, generating the 400 nm pump with a pulse energy of ~50 μJ. The pulse is compressed by a prism pair to ~40 fs and attenuated to ~0.5 μJ for excited-state FSRS (Fig. 3–5). This pump power was tested to be within the linear regime and also provide sufficient S_1 population.[4-7] The fs Raman probe is generated by focusing ~15 μJ FP on a 2-mm *Z*-cut single-crystal sapphire plate to produce the supercontinuum white light. Using a blaze in the prism compressor beampath, we select the wavelength range from ca. 585—650 nm that corresponds to ca. 100—1800 cm^{-1} Stokes Raman shift with the 580 nm Raman pump (e.g., see Fig. 1–3 for experimental spectra).

When the Raman pump wavelength is tuned toward electronic resonance, the excited-state FSRS signal intensity increases nonlinearly with the pump power due to depletion of excited-state population by the Raman pump through excited-state absorption (ESA, conversion to higher lying electronic states above PA*) or stimulated emission (SE, dumping to ground state PA).[8,9] For the 420 cm^{-1} mode (see Fig. 3a) of photoexcited HPTS in H_2O (pH = 4.5, Fig. S1a), the Raman pump power dependence was measured from ca. 0.5—10 mW. The time delay between the 400 nm actinic pump and broadband Raman probe is fixed at 100 fs. The observed excited-state vibrational mode intensity increases as a function of Raman pump power until ~4.5 mW after which the signal plateaus. Therefore, we set the 580 nm Raman pump at 4 mW for all the experiments in this work to achieve the optimal balance between signal strength and stability in the linear regime.[8,10] The PB^* modes are also pre-resonantly enhanced under this condition (see Fig. S4a for transient absorption, or TA spectra; and Fig. S4e for TA dynamics).

B. Data Processing Methods. Experimental spectral data are processed in IGOR Pro. The solvent and ground-state HPTS spectra are scaled and subtracted from the excited-state Raman spectrum at each time delay, resulting in pure vibrational modes on top of a smooth and largely featureless baseline (i.e., Raman pump-induced change to the TA lineshape). Spline baselines are drawn and subtracted from each time-dependent trace, yielding only the excited-state Raman signal (see Fig. 3 and Fig. S5). For kinetic analysis, individual vibrational modes in S_1 are least-squares fitted by a Gaussian curve with the output center frequency and integrated intensity plotted against time. The multi-exponential fit of each Raman mode intensity versus time is convoluted with the ~140 fs full-width-at-half-maximum (FWHM) instrument response function, measured from the cross correlation between the fs actinic pump and Raman probe pulses.[5,6,9]

ESI Text

A. Steady-State Electronic Spectroscopy of HPTS and MPTS. HPTS is a photoacid with pK_a of ~7 that drops to 0 following 400 nm irradiation.[5,11-16] It is generally accepted that the protonated form of aqueous HPTS in S_1 (PA*) undergoes excited state proton transfer (ESPT) and emits at ~514 nm from the deprotonated state (PB*). We measure the sample solution at several pH values; the ground-state FSRS data and UV/Visible spectra are shown in Fig. 1 and Fig. S1a, respectively. A small portion of the fluorescence signal centered at ~440 nm originates from PA*, and its contribution decreases with increasing pH and a larger population of deprotonated HPTS chromophore. The methoxy derivative of HPTS, MPTS, lacks an ionizable proton and cannot undergo ESPT,[5,16] so it shows no significant pH dependence in the absorption or emission spectrum from pH = 4.5 to 12 (Fig. S1b) with only one dominant fluorescence peak at ~435 nm from the trapped PA* state.

B. Ground-State FSRS of HPTS. In recent years, FSRS has been developed as a powerful technique to study vibrational structural dynamics with high temporal and spectral resolutions.[2,4,6,10,17] FSRS measures ground-state vibrational spectrum free from fluorescence background in comparison to conventional techniques such as continuous-wave (cw) spontaneous Raman spectroscopy. For example, with increased pH, HPTS vibrational frequency shift and peak enhancement in Fig. 1a confirm the acid-base transition because PB shows more resonance enhancement than PA under the 580 nm Raman pump (see Fig. S1a). The stimulated Raman spectra for HPTS in D_2O at various pD values (Fig. S2) show an array of peaks with high signal-to-noise ratio (SNR) from ca. 100—1800 cm^{-1} so a detailed comparison to the chromophore peaks in H_2O (Fig. 1a) can be made to discern the H/D isotope effect.

C. Low-Frequency Mode Assignment. To systematically characterize the low-frequency modes, ground-state FSRS spectra were collected on highly concentrated (4 M) halide salts (NaCl, NaBr, NaI) dissolved in H_2O to benchmark the sensitivity of FSRS in the low-frequency regime (Fig. 2). It has been reported that the ~180 cm^{-1} mode in aqueous solution is an intermolecular H-bond stretching mode (O–H···O).[18] The addition of halide salts to water changes the H-bonding structure of water as new ion-dipole interactions form, and we observe via ground-state FSRS measurement that the 180 cm^{-1} Raman mode redshifts and strengthens with increasing size and mass of the halide ions ($Cl^- < Br^- < I^-$) in aqueous solution.

This mode assignment is further substantiated by DFT calculations both in the electronic ground and excited state.[19] The major atomic displacements associated with the experimentally observed vibrational marker bands at ~180, 280, 420, 480, 1530, and 1560 cm^{-1} are depicted in Fig. S3. The calculated 426 cm^{-1} (protonated) and 471 cm^{-1} (deprotonated) modes show that the

four-ring skeletal motions are intricately correlated with deprotonation, e.g., the latter out-of-plane motion is enhanced in deprotonated chromophore likely due to more electron density shifting back toward the ring system.[5,13] The emerging 480 cm^{-1} mode at later time in Fig. 3a and Fig. S5a can be attributed to PB* formation in H_2O and D_2O, respectively. In addition, the calculated in-plane C=C stretching with strong COH rocking mode blueshifts from protonated (1531 cm^{-1}) to deprotonated (1542 cm^{-1}) chromophore of HPTS, corroborating the experimental observation (ca. 1530→1560 cm^{-1}) as ESPT converts PA* to PB* (Fig. 4a). Notably, the calculated mode frequencies in S_0 cannot fully reproduce the excited-state mode frequencies due to different electronic configuration and the non-equilibrium, coherent nature of the observed Raman modes in S_1. However, the close proximity of mode frequencies and overall trend should still hold for characteristic vibrational motions and frequency change as a result of ESPT.[6] Moreover, our experimental results may serve as benchmarks for theoretical efforts to calculate Raman mode frequencies and intensities starting from the Franck-Condon region when the photoexcited non-stationary wavepacket is most energetic, samples phase space, interacts with surrounding solvent molecules, and dissipates energy in the sub-ps to ps realm.[20-24]

D. Electronic Excited States and Tunable FSRS of HPTS. We perform excited-state FSRS on HPTS by tuning the Raman pump and probe wavelengths in the visible range to optimize the stimulated Raman signal strength. A strong TA-like background emerges that overwhelms FSRS signal when the Raman pump is tuned to 480—550 nm (see Fig. S4a-b), mainly due to the Raman pump depletion effect. In addition, complex TA dynamics including ESA and SE from both PA^* and PB^* states in this region may distort the FSRS signal. For instance, dispersive features at early time delay from hot luminescence terms can be observed if the Raman pump is

on resonance with the SE of PA* at ~440 nm (see Fig. S1).[25-27] Given that we collect excited-state Stokes Raman spectra in this work, the prudent choice of a 580 nm Raman pump to the red side of the ESA and SE features puts the Raman probe pulse further away from the electronic resonance, resulting in clearer and "cleaner" stimulated Raman features for quantitative analysis.

E. Transient Vibrational Dynamics from Excited-State FSRS. For HPTS in H_2O (D_2O) at pH=4.5 (pD=4.5), the 1530 cm^{-1} mode frequency blueshift exhibits double-exponential dynamics of 2.5 and 45 (7.0 and 130) ps with amplitude weight 34% and 66% (28% and 72%) as shown in Fig. 4a. This result is in accord with the stepwise vibrational evolution of ESPT from PA* to PB*[6,14] and a small time dwell in observing the PB* accumulation in S_1 after photoexcitation.[4] Notably, the ~30% relative amplitude weight of the first time constant is consistent with previous reports on the three-step ESPT model[6,14,28,29] that attributes the 3—4 ps process in aqueous solution to the formation of the contact ion pair such as $[R^*O^- \cdots H^+OH_2]$. This ion pair is not isolated in solution and has been suggested to further consist of tight and loose water complexes with unspecified number of water molecules in between the proton donor and acceptor.[15,30,31]

As a key feature for necessary solvent reorganization following photoexcitation of HPTS, adjacent water molecules particularly near the HPTS phenolic hydroxyl need to accommodate the primary coordination number change from four (for H_2O) to three (for H_3O^+) with the latter also known as the Eigen complex,[15,16,29-33] $H_3O^+(H_2O)_3$. It is conceivable that at the electronic ground state (S_0) and neutral to acidic pH, the phenolic hydroxyl group of HPTS is loosely bound to the nearby water molecule(s).[6] Once the proton starts to shift toward water due to increased acidity of HPTS* in S_1, the hydroxyl oxygen atom of the photoexcited chromophore becomes one of the oxygen atoms in the solvation structure for the newly formed hydronium ion

on the few ps timescale. Subsequently, the second and dominant blueshift time constant of the intramolecular 1530 cm^{-1} mode in H_2O is ~45 ps and exhibits an H/D KIE of ~3, so it reports on ESPT-related processes with a small activation barrier[6,15,16] but may involve other relaxation pathway contributions such as intermolecular vibrational cooling via H-bonds and thermal heat transfer (see Table 1, and the associated atomic motions in Fig. S3e-f). This is largely consistent with the 45 ps time constant retrieved from the PA* 180 cm^{-1} mode intensity decay (see Fig. 5a and Table 1) but the coincidental number match should not be attributed to same spectral origin. As a result, we did not list the 45/130 ps mode blueshift time constant in H_2O/D_2O in Table 1 because of the above-mentioned spectral overlap issues during PA*→PB* conversion and convoluted contributions from both ESPT reaction and vibrational cooling on the ps timescale.

Below 1000 cm^{-1}, the Raman modes report on transient skeletal motions involving multiple heavy atoms across the conjugated ring system of HPTS, providing further insights into the ESPT reaction coordinate.[4] As shown in Fig. 4b, the 420 cm^{-1} PA* intramolecular mode with its associated motion depicted in Fig. S3c decays with ~450 (500) fs, 2.7 (8) ps, and 90 (250) ps time constants for HPTS in H_2O (D_2O), respectively. The similar initial decay is due to vibronic wavepackets leaving the PA* Franck–Condon region likely with contributions from ultrafast vibrational cooling. The sub-ps time constant suggests that large-scale proton motion does not occur in this stage.[15,34] The subsequent decay components on the ps timescale indicate multi-stage proton motion in water, which is generally considered to involve the formation and separation of transient solute-solvent contact ion pairs.[6,14-16] In comparison, the ~480 cm^{-1} mode shows biexponential rise without the sub-ps component, suggesting that PB* significantly accumulates following (i.e., not during) the initial small-scale proton motions.[15,34,35] Moreover, the intramolecular vibrations of HPTS (e.g., 420 and 480 cm^{-1}) exhibit similar excited-state

dynamics in $H_2{}^{16}O$ and $H_2{}^{18}O$, indicating that the solvent isotope effect of $^{16}O/^{18}O$ does not significantly influence the ESPT rate of HPTS in aqueous solvents (Fig. S6).

In comparison to the PA* 180 cm^{-1} mode dynamics described in main text, the 280 cm^{-1} mode decays with ~450 (500) fs, 2.5 (8) ps, and 95 (250) ps time constants for HPTS in H_2O (D_2O), respectively, suggesting that this intramolecular ring deformation has a longer lifetime in S_1 (Fig. 3a) and more closely tracks ESPT dynamics than the intermolecular H-bond stretch (i.e., largely insensitive to the actual proton location between the two oxygen atoms).[36] The 180 cm^{-1} H-bonding mode initially sets up the stage for ESPT as a "tuning" or "gating" mode[4,37,38] and then helps vibrational cooling via its intermolecular solute-solvent interaction. In general, higher-frequency intramolecular mode intensities at ~280, 420, 480, and 1530 cm^{-1} track ESPT progress (see retrieved time constants in Table 1) as they are more sensitive to electron redistribution and conformational dynamics of the chromophore (with conjugated aromatic ring system)[5,6] but less sensitive to cooling via the intermolecular H-bonding chain at the phenolic hydroxyl end.

On the sub-ps timescale in water, Fig. 5c shows pronounced 280 cm^{-1} mode intensity quantum beats due to anharmonic vibrational coupling to the impulsively driven coherent 180 cm^{-1} mode in the excited state,[24,39,40] while experimental evidence of quantum beating[4,41,42] of the latter mode is less obvious. This is likely due to our time delay steps (50 fs within the first 1 ps) during excited-state FSRS data acquisition so the Nyquist frequency of ~330 cm^{-1} is close to 280 cm^{-1}. In addition, reduced SNR of the weaker 180 cm^{-1} H-bonding mode with small electric polarizability poses challenge to reliably resolve its coherent spectral oscillations on fs timescale.

Moreover, unlike GFP chromophores,[4,37,43] HPTS does not show significant oscillatory features in the high-frequency region. Besides spectral overlap between resonantly enhanced Raman peaks that hinders analysis of individual vibrational mode dynamics (see Fig. 3 and Fig.

S5 for example), the four conjugated rings of HPTS comprise a relatively rigid molecular framework so skeletal collective motions lead to less spatial and electron displacement hence the reduced conformational degrees of freedom and electric polarizability.[44] This property is in contrast to the two-ring system in GFP chromophore with a more flexible ethylenic bridge in between and more significant electron motions across the ring moieties, hence the notable spectral oscillations for high-frequency vibrational marker bands.[4,37]

F. Fate of the 180 cm^{-1} Mode Revealed by Time-Resolved FSRS. Following 400 nm photoexcitation and the initial formation of the proton-(partially)-transferred contact ion pair, the timeline of the 180 cm^{-1} intermolecular H-bond stretching mode can be summarized below. Starting in the ground state (S_0) with H-bond of the type [ROH···OH_2] the system then moves within the photoexcitation time to the electronic excited state (S_1 in this case for HPTS), where the H-bond is now of the "unsettled" form [R*OH···OH_2] and has stronger intensity than its S_0 counterpart (see Fig. 3a) due to increased Raman polarizability and/or resonance conditions. Next, following proton transfer the H-bond is initially within the proton-transferred contact ion pair [R*O^- ···H^+OH_2]. This newly formed H-bond should be stronger than the H-bond in the neutral complex before proton transfer has occurred. Subsequently, following the separation of the contact ion pair by diffusion (on the ~100 ps timescale in water, see main text) the H-bond will be in the form of [R*O^- ···OH_2] which should be weaker than the H-bond within the proton-transferred contact ion pair. This could be due to increased intermolecular distance between the two oxygen atoms,[45,46] as well as reduced Raman polarizability in a vibrationally relaxed state and/or less optimal resonance enhancement leading to decreased excited-state Raman mode intensity.[3,5,17] Finally, when the proton is solvated in bulk water, new H-bond interactions are

formed (still in S_1 prior to fluorescence on the hundreds of ps to ns timescale) which are not subtracted away by taking the bulk water background in the electronic ground state (S_0). Each fully solvated proton will form one very strong H-bond in the protonated water dimer (e.g., Zundel cation) or tetramer (e.g., Eigen cation with a hydronium core, which can interconvert with Zundel cation via quantum fluctuations, low-barrier H-bonds, and Grotthuss proton transfer)[14,32,33,47-49] and between 2—4 strong H-bonds of water interacting with the first shell water molecules directly solvating the proton from the chromophore.

Notably, the 180 cm^{-1} mode intensity dynamics (see Fig. 3a and 5a) show that we cannot observe a clear intermolecular H-bond stretching mode at ~600 ps after photoexcitation, still in the electronic excited state S_1 for HPTS chromophore, which merits some discussion. It is reasonable for the mode absence at photoexcitation time zero in H_2O (pH=12, Fig. 3a top trace) due to background subtraction (see main text), but for transient excited-state Raman data in H_2O (pH=4.5) PA* has a stronger, blueshifted peak at ~193 cm^{-1} at time zero (Fig. 5b). We can understand why the newly formed PB* H-bonds after ESPT cannot be readily observed by performing quantitative estimate from spectral data in Figures 1a and 3a. **(1)** If we assume that 600 ps represents sufficient time for the PB* H-bond (i.e., $[R^*O^- \cdots OH_2]$ as shown above) to form, the population (represented by concentration here) of PB* H-bonding mode near 180 cm^{-1} is $1.5\ mM \times 10\% \times 0.9 = 0.135\ mM$. This *upper-bound* estimate considers the typical 10% (see previous FSRS literature including ours)[2,4,5,17] $S_0 \rightarrow S_1$ population conversion by photoexcitation, and 90% PA*→PB* (high end estimate for QY, quantum yield) population conversion crossing the ESPT barrier. **(2)** Because 600 ps is likely sufficient time to form PB* H-bonds in a relaxed state (versus non-equilibrium, highly energetic, vibrationally hot wavepacket motion in the Franck-Condon region like the observed PA* H-bonding mode at ~180 cm^{-1} in Fig. 3a), it is

reasonable to estimate Raman gain for the PB* H-bond from the observed PB H-bond in Fig. 1a (i.e., [$RO^{-}\cdots HOH$], 0.45% stimulated Raman gain, using 40 mM HPTS). Therefore, the expected Raman gain magnitude for nascent PB* H-bonding mode is $0.45\%/40\ \text{mM}\times 0.135\ \text{mM} = 0.0015\%$. **(3)** Typical PA* H-bonding mode at ~180 cm^{-1} has a stimulated Raman gain of ~0.12% (see Fig. 3a), which is thus ~80 times stronger than the aforementioned PB* H-bonding mode assuming unchanged Raman polarizability from PA* to PB* H-bond. **(4)** If we take into consideration that Raman polarizability likely decreases as photoexcited molecules move out of the Franck-Condon region and reach a more relaxed state,[2,4,6,37] the PB* H-bonding mode intensity will be even lower at ~600 ps (e.g., at least two orders of magnitude smaller than the PA* H-bonding mode intensity before ~1 ps). Taken together, it explains why we did not observe the PB* H-bond mode near 180 cm^{-1} up to 600 ps, while we can retrieve the relatively clean PA* H-bond mode dynamics (Fig. 5a, b) and associated time constants (Table 1).

On a related note, in comparison to IR spectroscopy (either 1D or 2D)[33,50-52] that can use the O–H stretching vibration as a sensitive mode for proton hydration, time-resolved FSRS is more powerful in revealing lower frequency skeletal motions prior to and during ESPT starting from the Franck-Condon region. This type of non-equilibrium, multidimensional reaction coordinate dynamics inquiry is key to revealing primary molecular events facilitating ESPT — those transient vibrational modes benefit from enhanced Raman polarizability and/or resonance conditions that further increase the signal-to-noise ratio.[1,4,53] On the contrary, we expect the signal from fully hydrated proton in bulk water either in electronic excited state after hundreds of ps (see above) or in electronic ground state (e.g., thermal equilibrium, see Fig. 1a) to be rather small due to extensive H-bonding and reduced Raman polarizabilities in a more relaxed state,[44] which may not benefit from a time-resolved FSRS study without further signal enhancement.

G. Functional Relevance of the Observed Skeletal Motions. It is remarkable that in this work, the absence of a super-photoacid like the quinone-cyanine dye derivatives[45] with $pK_a^* < -8$ as the proton donor or a strong base like high concentration of acetate ions as proton acceptors[5,14] has enabled us to study ESPT in a relatively moderate condition: weak photoacid HPTS with $pK_a^* \approx 0$ in neat water. Being both the proton acceptor and solvation agent here, water plays a central role in the photochemical reaction pathway of HPTS. As a result, the optimization of local water H-bonding network surrounding the photoacid with the phenolic hydroxyl on one end and sulfonate groups on the other three ends becomes essential. This ultrafast phase-space search needs to occur in conjunction with the initial, highly directional proton movement along the H-bonding chain at the phenolic hydroxyl end,[34,46,53] which is reflected by the sub-ps vibrational dynamics of the 180 cm^{-1} intermolecular H-bond stretching mode (Fig. 5a-b). It is conceivable that the observed anharmonic coupling and the resultant coherent modulation of the 280 cm^{-1} four-ring deformation mode on the sub-ps to ps timescale reports on the effective rearrangement of H-bonding network within the first solvation shell of photoexcited HPTS molecule. These skeletal motions drive the formation of the contact ion pair [$R^*O^- \cdots H^+H_2O$] on the 3 ps timescale[6,15,16] which then undergoes diffusion-assisted separation and individual solvation events on the ~100 ps timescale in H_2O.

In other words, the functional importance of the coupled 180 and 280 cm^{-1} modes is deeply rooted in their cooperative ability to set up the stage for ESPT starting from time zero of photoexcitation,[4,5] particularly the formation of transient contact ion pair on the few ps timescale that essentially matches the observed vibrational coherent oscillations in ESPT-capable solvents (e.g., $H_2{}^{16}O$, $D_2{}^{16}O$, and $H_2{}^{18}O$) but not in methanol (see Fig. 5c insert) on the few ps timescale. The observed mode intensity oscillations are prominent on the sub-ps to ps timescale due to the

impulsive excitation nature of these low-frequency modes.[4,37,39] Our ensemble-averaged FSRS measurement in the electronic excited state effectively exposes dominant functional motions that survive stochastic fluctuations and/or cancellation effect. The tunable FSRS methodology thus provides a powerful platform to observe coherent modulation of excited-state vibrational modes (e.g., intensity, frequency) by other anharmonically coupled vibrational modes on the intrinsic lifetime of impulsively-excited coherent motions (typically on the 1—2 ps timescale in solution)[4,6,38] as long as the free induction decay (FID) of the reporter modes generated by the ps-Raman-pump-fs-Raman-probe pair is on par with or longer than the coherence timescale (i.e., impulsively driven by the fs actinic pump).

ESI Figures

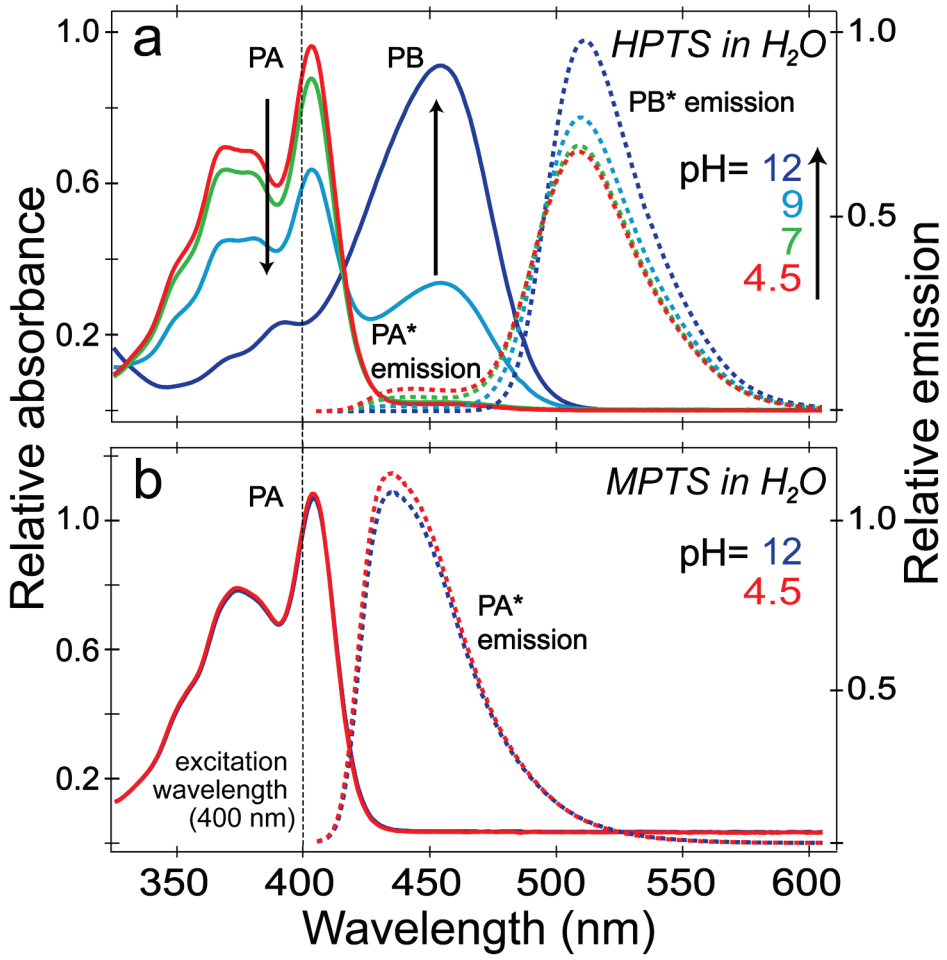

Fig. S1 Electronic absorption and emission spectra of HPTS and MPTS in water at different pH. (a) Steady-state absorption and emission spectra of 0.4 mM HPTS in aqueous solution (pH = 4.5, 7, 9, and 12). Protonated HPTS (PA) mainly absorbs at ~405 nm and emits around 440 nm. Increasing the solution pH from 4.5 to 12 causes the PA absorption band to decrease as the deprotonated photobase (PB) absorption band at 455 nm increases in intensity. The ESPT process from PA* to PB* eventually leads to dominant green emission centered at 514 nm. (b) Steady-state absorption and emission spectra of 0.4 mM MPTS in aqueous solution (pH = 4.5 and 12). Emission near 440 nm occurs from the trapped PA* state because it lacks ESPT capabilities due to the methoxy group without an ionizable proton.

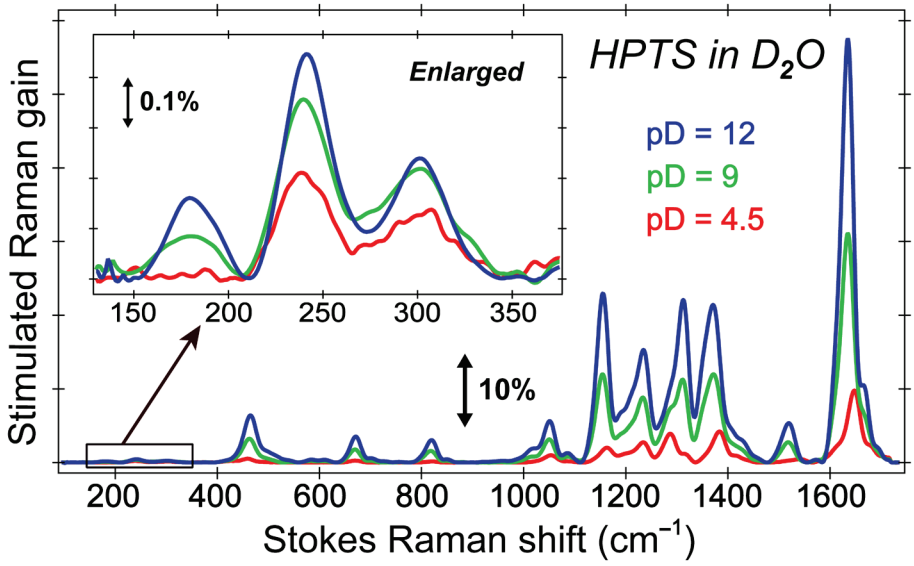

Fig. S2 Ground-state FSRS spectra of HPTS in D_2O at various pD conditions. The Stokes Raman spectrum in S_0 from 100—1700 cm^{-1} for 40 mM HPTS in D_2O at pD = 4.5 (red), 9 (green), and 12 (blue). The enlarged spectral region below 400 cm^{-1} is shown in the insert. The corresponding Raman gain magnitude is indicated by the double-arrowed line. Similar to the ground-state FSRS on HPTS in H_2O (Fig. 1a), the pH-dependent mode frequency shift and intensity change are observed. The ~180 cm^{-1} intermolecular H-bond stretching mode is absent at low pD values likely due to weak H-bonding interaction (see main text).

Notably, we used ~40 mM HPTS for ground-state FSRS (see Fig. 1a/S2 for HPTS in H_2O/D_2O) to enhance the Raman signal strength at thermal equilibrium, which enabled us to directly observe weak vibrational modes particularly in the low-frequency region (note that the 580 nm Raman pump is far away from the ground-state absorption peak of HPTS at ~400 nm, see Fig. S1, so the pre-resonance enhancement is insignificant). For time-resolved excited-state FSRS measurements, we intentionally used much lower concentration (i.e., 1.5 mM, see Figs. 3-5 caption) because the 580 nm Raman pump achieves much better resonance Raman effect by overlapping with excited-state electronic bands including both ESA and SE (see Fig. S4 below).

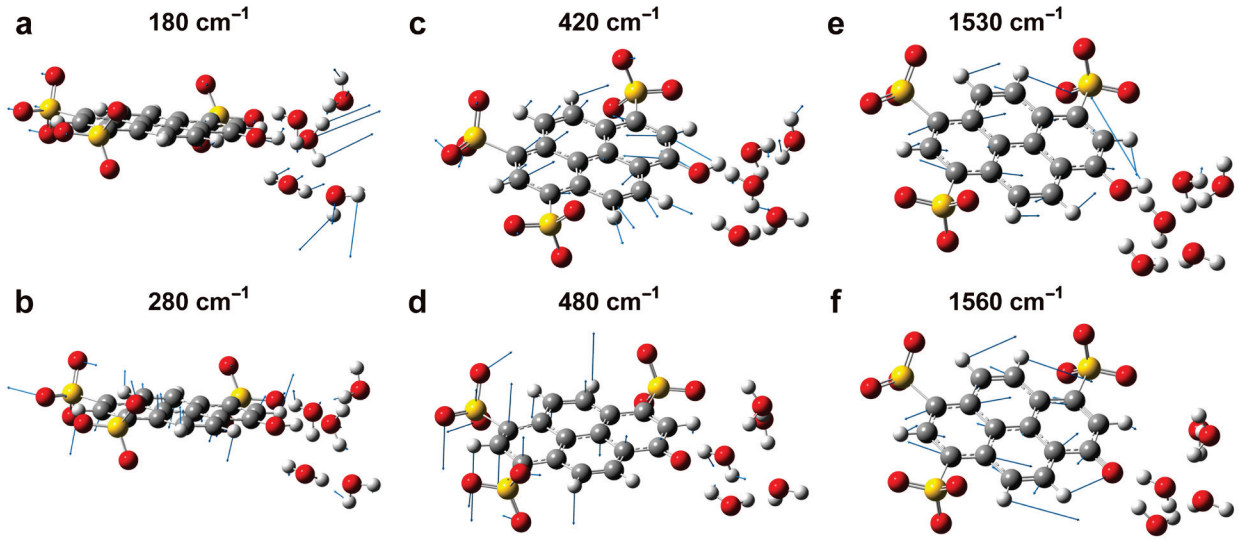

Fig. S3 Major vibrational motions of HPTS in water based on DFT calculations. Six calculated ground-state Raman modes are depicted with atomic displacement shown by blue arrows: (a) 166 cm^{-1} (protonated); (b) 264 cm^{-1} (protonated); (c) 426 cm^{-1} (protonated); (d) 471 cm^{-1} (deprotonated); (e) 1531 cm^{-1} (protonated); and (f) 1542 cm^{-1} (deprotonated chromophore). The frequency-scaling factor used is 0.98. The corresponding experimentally observed vibrational marker band frequencies in the electronic excited state (S_1) are noted above each representative motion (see ESI Text). The carbon, sulfur, oxygen, and hydrogen atoms are shown as grey, yellow, red, and white spheres, respectively. Five adjacent water molecules near the chromophore hydroxyl end are also quantum mechanically treated (see Experimental).

Given the anharmonicity of the molecular system, the mode assignments are provided as a simplified representation of realistically more complex vibrational motions of mixed character. However, the focus should be put on the frequency trend and characteristic nature that are associated with certain structural motifs and/or atomic motions, which assist our spectral analysis and mechanistic interpretation of the ground-state and excited-state FSRS data (see main text).

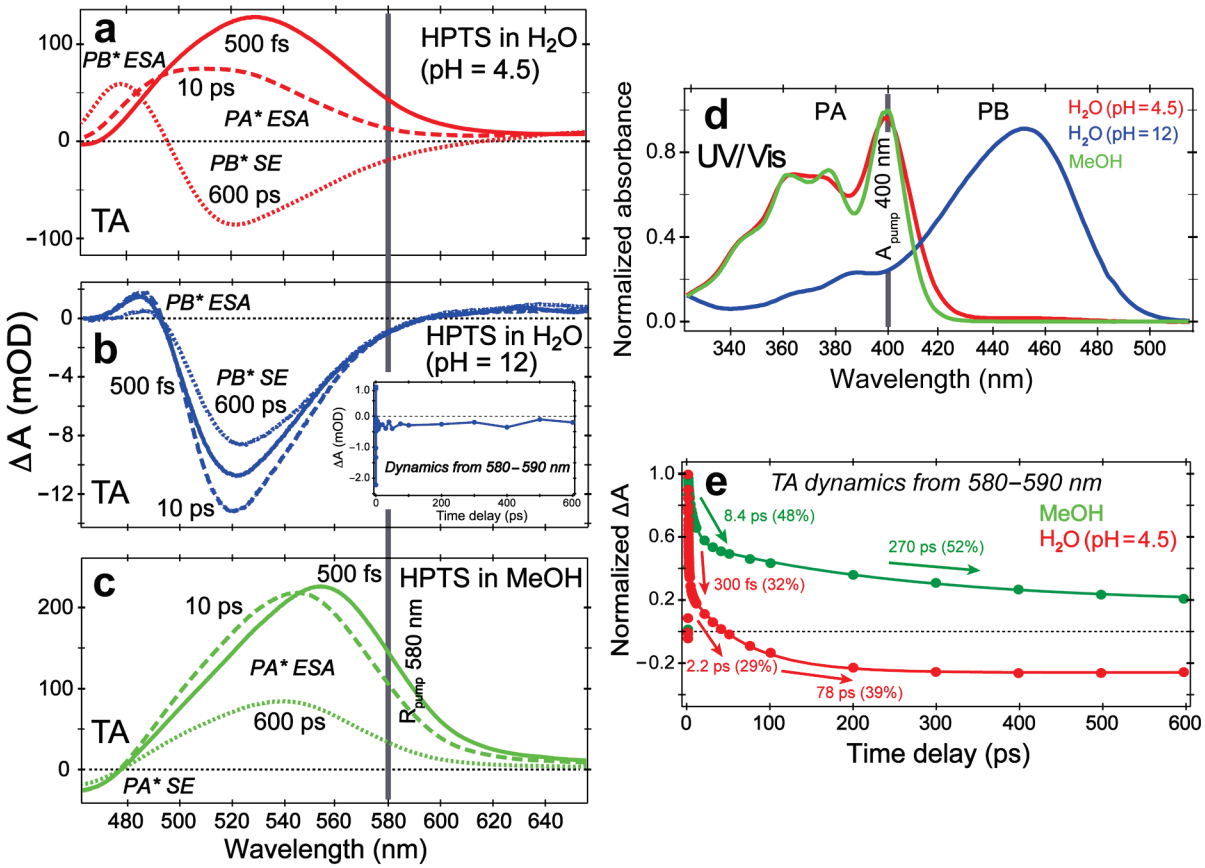

Fig. S4 Transient absorption (TA) spectra of HPTS in water and methanol. Femtosecond TA spectra of 0.4 mM HPTS in (a) pH = 4.5 aqueous solution; (b) pH = 12 aqueous solution; and (c) methanol at 500 fs (solid line), 10 ps (dashed line), and 600 ps (dotted line) following 400 nm photoexcitation. The vertical axis is in milli-optical density (mOD) units. The transient electronic state assignment for HPTS chromophore is noted. The Raman pump center wavelength position is indicated by the vertical gray bar. (d) Steady-state absorption spectra of 0.4 mM HPTS in H_2O at pH=4.5 (red) and 12 (blue) as well as in methanol (green). The actinic pump wavelength at 400 nm for excited-state FSRS is indicated by the vertical gray bar. Note, the much smaller ΔA value observed in (b) is consistent with inefficient pumping of PB species using 400 nm actinic pump as shown in (d).[5,6] (e) TA dynamics from 580—590 nm of HPTS in methanol (green) and H_2O (pH=4.5, red). Least-squares multi-exponential fit (solid traces) time constants and weights are listed for this appropriate range for R_{pu} (580 nm) and the Stokes condition ($R_{pr} > 580$ nm).

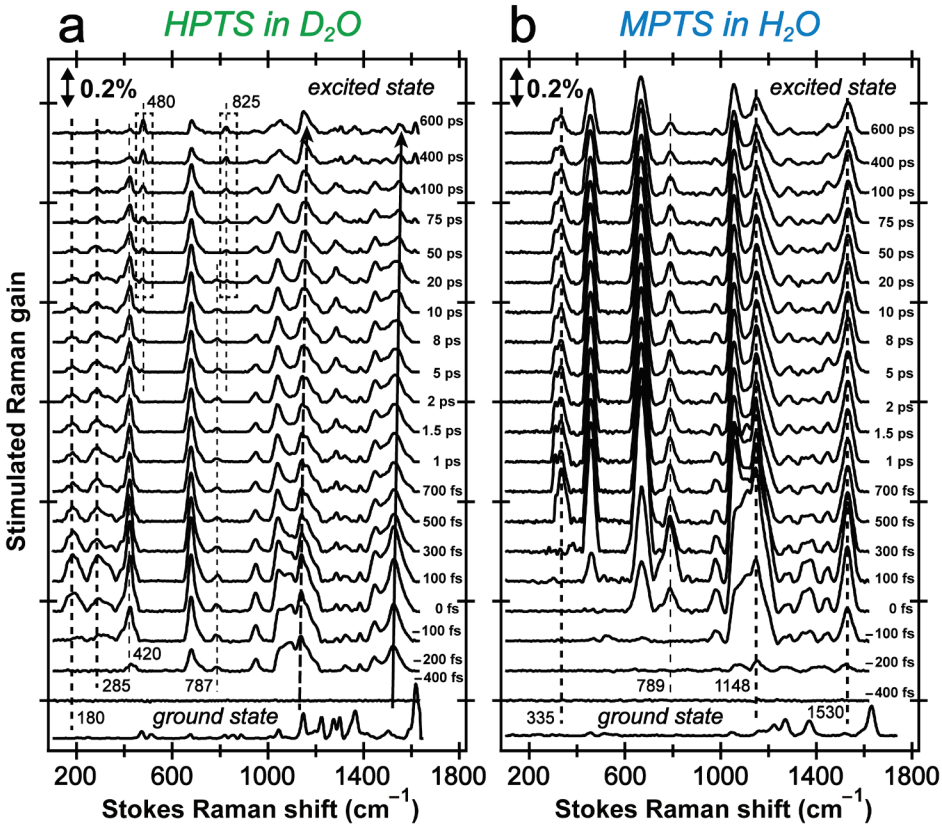

Fig. S5 Excited-state FSRS spectra of MPTS in H_2O and HPTS in D_2O. Time-resolved Stokes Raman spectra of (a) 1.5 mM HPTS in D_2O at pD=4.5 and (b) 1.5 mM MPTS in H_2O with 400 nm actinic pump for photoexcitation and 580 nm Raman pump across the detection window of ca. 100—1700 cm^{-1}. MPTS cannot undergo ESPT so only PA* modes (frequency unchanged) are observed within the 600-ps time window. The long-lived dynamics resemble HPTS in MeOH (Fig. 3b).[7,12] Proton transfer takes longer in D_2O than that in H_2O (Fig. 3a) due to kinetic H/D isotope effect (see ESI Text), and PB* modes (highlighted by dashed boxes) are not apparent until after ~50 ps. The blueshift of the ~1135 and 1530 cm^{-1} mode in (a) is highlighted by dashed and solid curved arrow, respectively, which can be compared to Fig. 4a. The stimulated Raman gain magnitude of 0.2% is indicated by the double-arrowed vertical line. The selected delay time point is noted on the right side of each time-resolved spectral trace. A number of vibrational marker bands are indicted by vertical dashed lines with frequencies labeled below in cm^{-1} units.

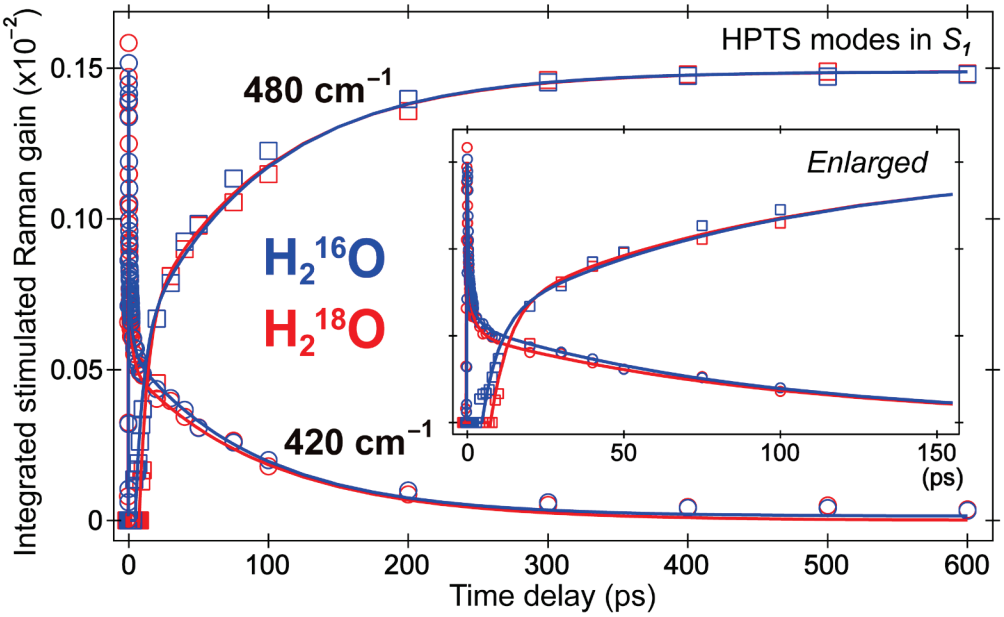

Fig. S6 Dynamics of vibrational marker bands of 1.5 mM photoexcited HPTS in $H_2{}^{16}O$ and $H_2{}^{18}O$ (pH=4.5). Intensity decay of the 420 cm^{-1} PA* mode (hollow circles) and rise of the 480 cm^{-1} PB* mode (hollow squares) are plotted for HPTS in $H_2{}^{16}O$ (blue) and $H_2{}^{18}O$ (red), respectively. The triple-exponential decay and double-exponential rise least-squares fitting results for the 420 and 480 cm^{-1} modes are shown in solid lines (see Table 1 for time constants and structural origin). No significant difference for the ESPT progress is observed. The enlarged time-resolved mode intensity plot within 150 ps is shown in the insert.

The integrated, stimulated Raman gain of the 420 cm^{-1} mode decays with three characteristic time constants of ~500 fs (57% amplitude weight), 3 ps (13% weight), and 90 ps (30% weight) in both water solvents. The 480 cm^{-1} mode intensity rises with two characteristic time constants of ~6 ps (40% weight) and 90 ps (60% weight) in both solvents (see Table 1), suggesting a small dwell for PB* accumulation from the initial decay of PA* as a consequence of the multi-stage ESPT reaction and the accompanying solvation dynamics of the proton-(partially)-transferred complex in water (see main text).[4,6]

ESI References

1 L. Zhu, W. Liu and C. Fang, *Appl. Phys. Lett.*, 2014, **105**, 041106.

2 R. R. Frontiera, C. Fang, J. Dasgupta and R. A. Mathies, *Phys. Chem. Chem. Phys.*, 2012, **14**, 405-414.

3 A. B. Myers and R. A. Mathies, in *Biological Applications of Raman Spectroscopy*, ed. T. G. Spiro, John Wiley & Sons, Inc., New York, 1987, vol. 2, pp. 1-58.

4 C. Fang, R. R. Frontiera, R. Tran and R. A. Mathies, *Nature*, 2009, **462**, 200-204.

5 W. Liu, F. Han, C. Smith and C. Fang, *J. Phys. Chem. B*, 2012, **116**, 10535-10550.

6 F. Han, W. Liu and C. Fang, *Chem. Phys.*, 2013, **422**, 204-219.

7 Y. Wang, W. Liu, L. Tang, B. G. Oscar, F. Han and C. Fang, *J. Phys. Chem. A*, 2013, **117**, 6024-6042.

8 J. Lee, J. R. Challa and D. W. McCamant, *J. Raman Spectrosc.*, 2013, **44**, 1263-1272.

9 F. Han, W. Liu, L. Zhu, Y. Wang and C. Fang, *J. Mater. Chem. C*, 2016, **4**, 2954-2963.

10 D. W. McCamant, P. Kukura, S. Yoon and R. A. Mathies, *Rev. Sci. Instrum.*, 2004, **75**, 4971-4980.

11 E. Pines, D. Huppert and N. Agmon, *J. Chem. Phys.*, 1988, **88**, 5620-5630.

12 N. Agmon, D. Huppert, A. Masad and E. Pines, *J. Phys. Chem.*, 1991, **95**, 10407-10413.

13 T.-H. Tran-Thi, T. Gustavsson, C. Prayer, S. Pommeret and J. T. Hynes, *Chem. Phys. Lett.*, 2000, **329**, 421-430.

14 M. Rini, B.-Z. Magnes, E. Pines and E. T. J. Nibbering, *Science*, 2003, **301**, 349-352.

15 P. Leiderman, L. Genosar and D. Huppert, *J. Phys. Chem. A*, 2005, **109**, 5965-5977.

16 D. B. Spry, A. Goun and M. D. Fayer, *J. Phys. Chem. A*, 2007, **111**, 230-237.

17 P. Kukura, D. W. McCamant and R. A. Mathies, *Annu. Rev. Phys. Chem.*, 2007, **58**, 461-488.

18 I. A. Heisler and S. R. Meech, *Science*, 2010, **327**, 857-860.

19 M. J. Frisch, G. W. Trucks, H. B. Schlegel, G. E. Scuseria, M. A. Robb, J. R. Cheeseman, G. Scalmani, V. Barone, B. Mennucci, G. A. Petersson, H. Nakatsuji, M. Caricato, X. Li, H. P. Hratchian, A. F. Izmaylov, J. Bloino, G. Zheng, J. L. Sonnenberg, M. Hada, M. Ehara, K. Toyota, R. Fukuda, J. Hasegawa, M. Ishida, T. Nakajima, Y. Honda, O. Kitao, H. Nakai, T. Vreven, J. J. A. Montgomery, J. E. Peralta, F. Ogliaro, M. Bearpark, J. J. Heyd, E. Brothers, K. N. Kudin, V. N. Staroverov, R. Kobayashi, J. Normand, K. Raghavachari, A. Rendell, J. C. Burant, S. S. Iyengar, J. Tomasi, M. Cossi, N. Rega, J. M. Millam, M. Klene, J. E. Knox, J. B. Cross, V. Bakken, C. Adamo, J. Jaramillo, R. Gomperts, R. E. Stratmann, O. Yazyev, A. J. Austin, R. Cammi, C. Pomelli, J. W. Ochterski, R. L. Martin, K. Morokuma, V. G. Zakrzewski, G. A. Voth, P. Salvador, J. J. Dannenberg, S. Dapprich, A. D. Daniels, Ö. Farkas, J. B. Foresman, J. V. Ortiz, J. Cioslowski and D. J. Fox, *Gaussian 09, Revision B.1,* Gaussian, Inc., Wallingford, CT, 2009.

20 J. D. Coe, B. G. Levine and T. J. Martínez, *J. Phys. Chem. A*, 2007, **111**, 11302-11310.

21 T. Ishida and P. J. Rossky, *J. Phys. Chem. B*, 2008, **112**, 11353-11360.

22 R. J. D. Miller, *Science*, 2014, **343**, 1108-1116.

23 X. Xu, J. Zheng, K. R. Yang and D. G. Truhlar, *J. Am. Chem. Soc.*, 2014, **136**, 16378-16386.

24 G. Batignani, G. Fumero, S. Mukamel and T. Scopigno, *Phys. Chem. Chem. Phys.*, 2015, **17**, 10454-10461.

25 D. W. McCamant, P. Kukura and R. A. Mathies, *J. Phys. Chem. B*, 2005, **109**, 10449-10457.

26 R. R. Frontiera, S. Shim and R. A. Mathies, *J. Chem. Phys.*, 2008, **129**, 064507.

27 K. Niu, B. Zhao, Z. Sun and S.-Y. Lee, *J. Chem. Phys.*, 2010, **132**, 084510.

28 R. Gepshtein, P. Leiderman, L. Genosar and D. Huppert, *J. Phys. Chem. A*, 2005, **109**, 9674-9684.

29 M. J. Cox and H. J. Bakker, *J. Chem. Phys.*, 2008, **128**, 174501.

30 O. F. Mohammed, D. Pines, J. Dreyer, E. Pines and E. T. J. Nibbering, *Science*, 2005, **310**, 83-86.

31 B. J. Siwick and H. J. Bakker, *J. Am. Chem. Soc.*, 2007, **129**, 13412-13420.

32 M. Eigen, *Angew. Chem. Int. Ed.*, 1964, **3**, 1-72.

33 M. Thämer, L. De Marco, K. Ramasesha, A. Mandal and A. Tokmakoff, *Science*, 2015, **350**, 78-82.

34 L. Tang, W. Liu, Y. Wang, Y. Zhao, B. G. Oscar, R. E. Campbell and C. Fang, *Chem. Eur. J.*, 2015, **21**, 6481-6490.

35 O. F. Mohammed, J. Dreyer, B.-Z. Magnes, E. Pines and E. T. J. Nibbering, *ChemPhysChem*, 2005, **6**, 625-636.

36 L. Genosar, P. Leiderman, N. Koifman and D. Huppert, *J. Phys. Chem. A*, 2004, **108**, 1779-1789.

37 B. G. Oscar, W. Liu, Y. Zhao, L. Tang, Y. Wang, R. E. Campbell and C. Fang, *Proc. Natl. Acad. Sci. U.S.A.*, 2014, **111**, 10191-10196.

38 D. P. Hoffman and R. A. Mathies, *Acc. Chem. Res.*, 2016, **49**, 616-625.

39 Y.-X. Yan, E. B. Gamble and K. A. Nelson, *J. Chem. Phys.*, 1985, **83**, 5391-5399.

40 D. T. Valley, D. P. Hoffman and R. A. Mathies, *Phys. Chem. Chem. Phys.*, 2015, **17**, 9231-9240.

41 M. H. Vos, F. Rappaport, J.-C. Lambry, J. Breton and J.-L. Martin, *Nature*, 1993, **363**, 320-325.

42 A. H. Zewail, *Femtochemistry: Ultrafast Dynamics of the Chemical Bond*, World Scientific, Singapore, 1994.

43 S. R. Meech, *Chem. Soc. Rev.*, 2009, **38**, 2922-2934.

44 J. L. McHale, *Molecular Spectroscopy*, Prentice-Hall, Upper Saddle River, NJ, 1999.

45 R. Simkovitch, S. Shomer, R. Gepshtein and D. Huppert, *J. Phys. Chem. B*, 2015, **119**, 2253-2262.

46 Y. Wang, L. Tang, W. Liu, Y. Zhao, B. G. Oscar, R. E. Campbell and C. Fang, *J. Phys. Chem. B*, 2015, **119**, 2204-2218.

47 J. T. Hynes, *Nature*, 1999, **397**, 565-567.

48 D. Marx, M. E. Tuckerman, J. Hutter and M. Parrinello, *Nature*, 1999, **397**, 601-604.

49 F. Garczarek and K. Gerwert, *Nature*, 2006, **439**, 109-112.

50 K. J. Gaffney, P. H. Davis, I. R. Piletic, N. E. Levinger and M. D. Fayer, *J. Phys. Chem. A*, 2002, **106**, 12012-12023.

51 E. T. J. Nibbering, H. Fidder and E. Pines, *Annu. Rev. Phys. Chem.*, 2005, **56**, 337-367.

52 R. M. Hochstrasser, *Proc. Natl. Acad. Sci. U.S.A.*, 2007, **104**, 14190-14196.

53 L. Tang, W. Liu, Y. Wang, L. Zhu, F. Han and C. Fang, *J. Phys. Chem. Lett.*, 2016, **7**, 1225-1230.